



TECHNICAL REPORTS: DATA

10.1029/2021GC010032

New Paleointensity Data From Aniakchak Volcano, Alaska, USA

Geoffrey Cromwell^{1,2}  and Yiming Zhang^{1,3} 

¹Occidental College, Los Angeles, CA, USA, ²Now at U.S. Geological Survey, California Water Science Center, Santa Maria, CA, USA, ³Now at University of California Berkeley, Berkeley, CA, USA

Key Points:

- We report the first set of absolute paleointensity data from Aniakchak volcano, Alaska, USA
- Glassy volcanic material yield high-quality results and were evaluated using strict selection criteria
- The new data fill in a gap of Holocene-age absolute paleointensity records from mid- to high-latitudes in North America

Correspondence to:

G. Cromwell,
geoffrey.cromwell@gmail.com;
gcromwell@usgs.gov

Citation:

Cromwell, G., & Zhang, Y. (2021).
New paleointensity data from
Aniakchak volcano, Alaska, USA.
Geochemistry, Geophysics, Geosystems,
22, e2021GC010032. <https://doi.org/10.1029/2021GC010032>

Received 19 JUL 2021

Accepted 30 SEP 2021

Author Contributions:

Conceptualization: Geoffrey Cromwell, Yiming Zhang
Data curation: Geoffrey Cromwell, Yiming Zhang
Formal analysis: Geoffrey Cromwell, Yiming Zhang
Funding acquisition: Geoffrey Cromwell, Yiming Zhang
Investigation: Geoffrey Cromwell, Yiming Zhang
Methodology: Geoffrey Cromwell, Yiming Zhang
Project Administration: Geoffrey Cromwell, Yiming Zhang
Resources: Geoffrey Cromwell, Yiming Zhang
Supervision: Geoffrey Cromwell, Yiming Zhang

Abstract This study presents the first set of Holocene, high-quality absolute paleointensity data from Alaska, USA. Existing paleointensity data for the Holocene are generally located at mid-northern latitudes in North America, Europe, the Middle East, and eastern Asia. Relatively few data are from the Alaska region. IZZI-modified paleointensity experiments were conducted on glassy volcanic materials from Aniakchak volcano, a mid- to high-latitude composite volcano on the Alaska-Aleutian arc. The CCRIT selection criteria were applied to the paleointensity results. A total of 30 specimens from six samples with estimated ages ranging from 1931 CE to 2,300 years before present passed all selection criteria. The sample-mean paleointensities ranged from 49.5 to 68.0 microTesla (μT). The sample-mean paleointensity results are comparable to modeled intensities, however all except for one sample-mean paleointensity are lower than those predicted by geomagnetic field models. The paleointensity estimate for the historical 1931 CE eruption was about 15 μT greater than the expected field strength. This overestimate may result from unrecognized alteration or non-ideal remanence carriers in this sample. Further evaluation of samples from the 1931 CE eruption using a Bayesian estimation method resulted in a paleointensity estimate that encompasses the historical field strength within uncertainty. These new paleointensity results are a valuable contribution to the mid- to high-northern latitude paleomagnetic data set. Incorporation of these data into future geomagnetic field models will improve the predictions of geomagnetic field behavior in the Alaska region.

1. Introduction

Reconstructing the Holocene evolution of Earth's magnetic field is important for understanding geodynamo processes in Earth's core, for studying long-term solar-terrestrial relationships, and for providing useful age constraints for archeological and stratigraphic units. There are several observation-based, continuous global geomagnetic field models (Constable et al., 2016; Korte & Constable, 2011; Korte et al., 2009, 2011; Nilsson et al., 2014; Pavón-Carrasco et al., 2014) that have various reconstructions and predictions of paleodirection and absolute paleointensity using historical measurements of the geomagnetic field and paleomagnetic data from archeomagnetic, volcanic, and sedimentary materials. Depending on the availability of spatially and temporally distributed reliable paleomagnetic data, the accuracy and resolution of different models of the past geomagnetic field can vary. Currently the majority of the Holocene archeomagnetic and volcanic paleointensity data come from mid-northern latitudes (30°N to about 50°N) in North America, Europe, the Middle East, and eastern Asia (Brown, Donadini, Korte, et al., 2015; Brown, Donadini, Nilsson, et al., 2015), biasing the models toward better resolution in these regions and lower resolutions in the higher latitudes and in the southern hemisphere. To improve future geomagnetic field models, it is essential to add more high-quality paleomagnetic data from areas with few current data points.

An under-represented region in the current paleomagnetic database is Alaska, especially along the volcanically active Alaska-Aleutian arc. Previous paleomagnetic studies in Alaska have mostly focused on tectonic questions on mainland Alaska (Hillhouse & Grommé, 1980; Packer & Stone, 1974; Stamatakis et al., 2001; Thrupp & Coe, 1986), or paleosecular variation studies on volcanoes along the Alaska-Aleutian arc (Bingham & Stone, 1972; Stone & Layer, 2006; Stone & Packer, 1979) and on Nunivak Island (Coe et al., 2000; Johnson et al., 2008). Paleointensity records from Alaska are limited, especially absolute paleointensity records. Previous studies focused on determining the relative paleointensity records from sediment cores with the purpose of better constraining the regional chronostratigraphy of the western Arctic (Barletta et al., 2008; Lisé-Pronovost et al., 2009). Stone and Layer (2006) conducted absolute paleointensity experiments using the Thellier-Coe method (Coe, 1967) on lava flows from the Aleutian Islands. However, only two samples from a *ca.* 2 Ma lava flow

© 2021. The Authors.

This is an open access article under the terms of the [Creative Commons Attribution-NonCommercial-NoDerivs License](https://creativecommons.org/licenses/by-nc-nd/4.0/), which permits use and distribution in any medium, provided the original work is properly cited, the use is non-commercial and no modifications or adaptations are made.

Visualization: Geoffrey Cromwell,
Yiming Zhang
Writing – original draft: Geoffrey
Cromwell, Yiming Zhang
Writing – review & editing: Geoffrey
Cromwell, Yiming Zhang

and one sample from a *ca.* 50 ka lava flow yielded acceptable paleointensity results. An evaluation of the efficacy of paleointensity experiments on pyroclastic-flow material from the historical 1912 CE. Novarupta volcano was conducted by Bowles et al. (2015). Sparse temporal coverage, and low success rate for absolute paleointensity records have limited systematic interpretation of the geomagnetic field behavior over the Alaska-Aleutian arc region.

Nevertheless, volcanoes of the Alaska-Aleutian arc are promising targets for northern mid- to high-latitude paleointensity investigations because of the active volcanism along the arc, availability of detailed geologic maps, and the preservation of fresh, glassy volcanic materials which can be faithful paleointensity recorders (Cromwell et al., 2018; Cromwell, Tauxe, & Halldórsson, 2015; Cromwell, Tauxe, Staudigel, & Ron, 2015). Aniakchak volcano, an active Pleistocene-Holocene composite volcano, is one such target (Figure 1). The volcano has undergone at least one caldera-forming eruption in postglacial time and last erupted in 1931 CE (Bacon et al., 2014). Aniakchak volcano contains glassy volcanic materials and has an established stratigraphic record that is calibrated based on ¹⁴C radiocarbon geochronology constraints from organic materials within or between eruptive materials (Bacon et al., 2014). No previous paleomagnetic studies have been conducted on Aniakchak volcano.

Glassy volcanic materials from Aniakchak volcano can be ideal targets for paleointensity experiments because single domain stable magnetic minerals tend to form during rapid cooling and often yield ideal paleointensity behaviors (Dunlop, 2005; Tauxe & Staudigel, 2004). A previous paleointensity study successfully obtained high-quality paleointensity estimates using submarine basaltic glass as old as 92 Ma (Tauxe & Staudigel, 2004). More recent paleointensity studies on glassy volcanic materials, decades to centuries to tens of thousands of years old, that formed from sub-aerial and sub-glacial eruptions have recovered accurate and high-quality estimates of geomagnetic field strength (Cai et al., 2017; Cromwell et al., 2018; Cromwell, Tauxe, & Halldórsson, 2015; Cromwell, Tauxe, Staudigel, & Ron, 2015). In this study, we conduct IZZI-modified paleointensity experiments (Tauxe & Staudigel, 2004) on glassy volcanic materials from Aniakchak volcano. Our data add to the observational records of the geomagnetic field strength at mid- to high-northern latitudes in Alaska during the Holocene.

2. Geologic Setting

The Alaska-Aleutian arc is an active chain of volcanoes that formed in the Eocene (Jicha et al., 2006) as a result of subduction of the Pacific Plate under the North American Plate. Aniakchak volcano is a Pleistocene-Holocene composite volcano located in the eastern part of the Alaska-Aleutian arc on the Alaska Peninsula (at approximately 56.9°N, -158.2°E), about 670 km southwest of Anchorage, Alaska (Figure 1). Aniakchak has been an active volcano since the last glacial period, having experienced multiple sub-Plinian to Plinian eruptions. The earliest Holocene Aniakchak eruption has been dated with radiocarbon method to have occurred between *ca.* 9,500 and 7,000 years before present (years BP; VanderHoek, 2009), and the latest eruption was a sub-Plinian eruption in 1931 CE.

Aniakchak volcano has been the subject of several geologic investigations, the most comprehensive one being a report on the postglacial eruption history, geochemistry and recent seismicity of the volcano by Bacon et al. (2014). Bacon et al. (2014) built upon previous investigations of the eruptive history of the volcano (Miller & Smith, 1977, 1987; Neal et al., 1992; VanderHoek, 2009; VanderHoek & Myron, 2004), specific eruptive and geologic events (Begét et al., 1992; McGimsey et al., 1994), potential volcanic hazards (Neal et al., 2000), and the geochemistry, petrology and magma evolution of the volcano (Dreher et al., 2005; George, 2004; Symonds et al., 2003). Pearce et al. (2017) used tephra from a radiocarbon-dated Aniakchak eruption to constrain the chronology of submarine sediments. The earliest reports specific to Aniakchak were by Smith (1925), who published the first geologic map of the crater, and by Hubbard (1931), who visited Aniakchak before and after the historical 1931 CE eruption. This investigation of paleointensity will be the first paleomagnetic investigation of Aniakchak volcano.

Aniakchak volcano has had two major postglacial eruptions (Miller & Smith, 1987). Aniakchak I is the oldest known eruption and the age of its andesite ignimbrite deposits has been bracketed by the timing of deglaciation around 9,500 years BP and ¹⁴C ages of *ca.* 7,000 years BP of organic materials beneath stratigraphically younger pumice-fall deposits (VanderHoek, 2009). The other major eruption, named Aniakchak II, is estimated to have occurred *ca.* 3,430 ± 70 years BP based on ¹⁴C ages of charcoal within an ignimbrite emplaced during the event (Bacon et al., 2014; Miller & Smith, 1987). The Aniakchak II event formed the outer boundary of the present-day

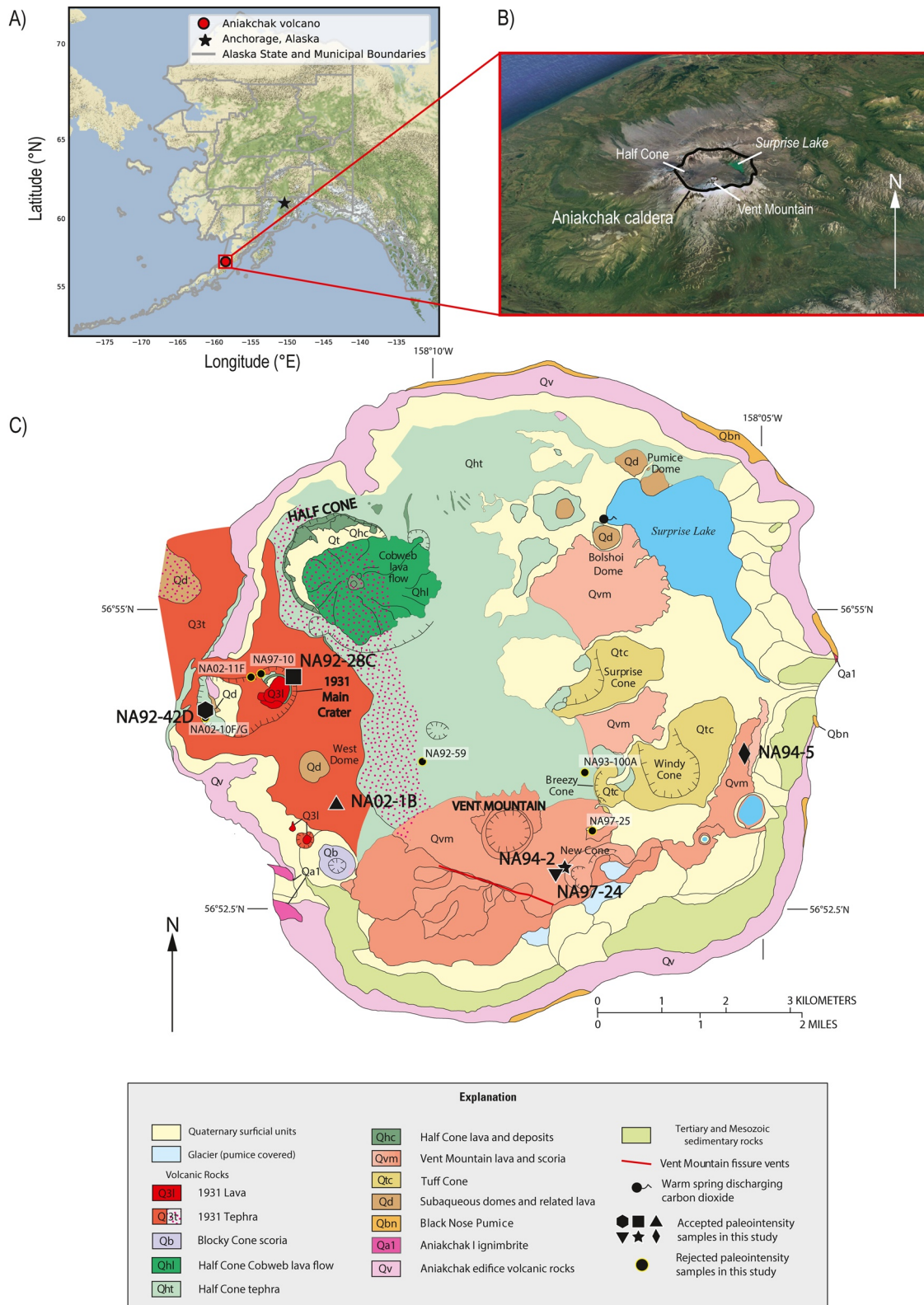


Figure 1. Regional setting of Aniakchak volcano. (a) Location of Aniakchak volcano with respect to the State of Alaska, USA, the city of Anchorage, and municipal boundaries; (b) perspective view of Aniakchak volcano (GoogleEarth imagery); (c) geologic map of Aniakchak caldera with locations of paleointensity sample used in this study. Map was modified from Bacon et al. (2014).

Aniakchak caldera (Figure 1). Multiple following eruptive events after the Aniakchak II eruption are summarized in detail by Bacon et al. (2014) and illustrated in Figure 1. The post-Aniakchak II record is complicated by a caldera lake having been present for part of this period, and little information is known about the earliest post-caldera materials prior to the emplacement of the dacite domes (unit Qd; Figure 1; Bacon et al., 2014). From the oldest to youngest, Bacon et al. (2014) describe the post-Aniakchak II geologic history to consist of subaqueous lava effusions forming dacite domes and related lava (Qd), catastrophic draining of the caldera lake, subsequent hydromagmatic eruptions forming the tuff cones (Qtc), later effusive and explosive eruptions that resulted in the formation of lava and scoria from Vent Mountain (Qvm), Half Cone (Qhc, Qht, and Qhl), and scoria from Blocky Cone (Qb). Finally, the 1931 CE eruption of tephra (Q3t) and lava flows (Q3l). Some of the post-Aniakchak II eruptive materials are overlain by glaciers and surficial deposits.

3. Sample Collection

Unoriented hand-samples were collected by the U.S. Geological Survey (USGS) Alaska Volcano Observatory in Anchorage, Alaska as part of an effort to document the eruption history of Aniakchak volcano. This effort included conducting ^{14}C radiometric age dating of organic materials to provide chronological control for the stratigraphic sections of the volcano and conducting detailed geochemical analyses to document the magmatic processes associated with Aniakchak eruptions (Bacon et al., 2014). For this study, 13 samples of those collected by the USGS were acquired for paleointensity experiments from the Geologic Materials Center (2015) in Anchorage, Alaska. Sample location information, descriptions, geologic unit assignments, and age estimates are listed in Table 1. Age estimates for each sample were interpreted for this study, all other information in Table 1 was previously published in Bacon et al. (2014) or available from the Geologic Materials Center (2015). The original sample names used by Bacon et al. (2014) and the Geologic Materials Center (2015) are retained in this study. The samples included in this study are post-Aniakchak II eruptive materials and range in age from *ca.* 2,300 years BP to 1931 CE.

3.1. Stratigraphy and Age Constraints

Age constraints for the samples included in this study were interpreted based on sample descriptions and stratigraphic and radiometric age constraints reported by Bacon et al. (2014), or summarized therein. The estimated ages of volcanic materials in Aniakchak volcano were acquired through ^{14}C dating on organic materials found in between tephra layers and lava flows in addition to stratigraphic relationships (Bacon et al., 2014). The interpreted age estimates for each sample are based on the geologic unit of each sample, ^{14}C age estimates of volcanic materials, and stratigraphic descriptions (Table 1). Geologic unit assignments for all samples are from Bacon et al. (2014), except for samples NA02-10F and NA02-11F which are interpreted for this study based on their location information and descriptions. Additional evaluation of the geochemical data of Bacon et al. (2014) (Figure 2) may help constrain the age of selected samples. Ages reported by Bacon et al. (2014), and used in this study, are given in radiocarbon years before 1950 CE. In this section we briefly describe the location, geologic unit, and estimated ages for each sample used in our paleointensity experiments.

3.1.1. Subaqueous Domes (Unit Qd)

Samples NA92-42D and NA02-10G were collected from the subaqueous domes and related lava flows (unit Qd; Figure 1) and have an estimated age range of 2,300–1,860 years BP (Table 1). The subaqueous domes are the oldest known products of post-Aniakchak II caldera-forming volcanism that were effused in an ancient caldera lake, of which modern Surprise Lake is a remnant (Figure 1; Bacon et al., 2014). The ancestral caldera lake was estimated to have catastrophically drained prior to $1,860 \pm 30$ years BP based on radiocarbon ages on wood from above sediment near the Aniakchak River mouth of $1,860 \pm 30$ years BP (Bacon et al., 2014; VanderHoek & Myron, 2004), thereby providing a minimum age constraint for emplacement of the subaqueous domes. A *ca.* 2,300 years BP pumice fall (derived from a radiocarbon age of $2,300 \pm 80$ years BP from Bacon et al. [2014]) is tentatively considered by Bacon et al. (2014) to have preceded, or to be contemporaneous with the emplacement of the subaqueous domes, thereby providing a maximum age constraint for the subaqueous domes.

3.1.2. Tuff Cone (Unit Qtc)

Sample NA94-5 was collected from Tuff Cone (unit Qtc; Figure 1) and has an estimated age range of 900–1,860 years BP (Table 1; Bacon et al., 2014). Radiocarbon dating of a soil above a tephra with Surprise Cone-like chemistry yielded a weighted mean age of 900 ± 80 years BP (Bacon et al., 2014), which is interpreted to provide

Table 1
Table of Location Information, Field Observations, Estimated Ages, Absolute Paleointensity Results, and Calculated VADM Values for All Samples

Sample	Lat	Lon	Age	Unit	m/n	B_F	$B_F\sigma$	VADM	VADM σ	Sample location and description
NA92-42D	56.9026	-158.2243	1,860 - 2,300	Qd	6/7	57.6	5.02	8.45E + 22	7.37E + 21	1931 Main Crater, west wall; pre-Half Cone, dense, gray, sparsely porphyritic lava flow, platy jointing
NA02-10G	56.9015	-158.2244	1,860 - 2,300	Qd	-/7	-	-	-	-	1931 Main Crater, west wall; dense gray lava flow with platy jointing high in west 1931 crater wall
NA94-5	56.8951	-158.0882	900 - 1,860	Qtc?	5/9	49.5	4.34	7.26E + 22	6.37E + 21	Lowest flow terrace below big maar; older lava flow near The Gates; possible Windy Cone source
NA94-2	56.8793	-158.1358	400±30	Qvm	6/6	57.0	3.65	8.37E + 22	5.36E + 21	New Cone rim, southeast flank of Vent Mountain; dark brown, scoriaceous, porphyritic pumice
NA97-24	56.8800	-158.1340	400±30	Qvm	6/7	58.8	1.91	8.63E + 22	2.80E + 21	East rim New Cone crater; New Cone agglutinate
NA97-25	56.8859	-158.1248	400±30	Qvm	-/6	-	-	-	-	Alluvial flat east of Vent Mountain; Vent Mountain lava, possibly related to New Cone
NA93-100A	56.8939	-158.1294	840 - 900	Qvm	2/7	-	-	-	-	East base of Vent Mountain; Vent Mountain lava younger than tuff cones, at base of tephra section
NA92-28C	56.9076	-158.2019	380±50	Qht	4/6	62.0	4.34	9.09E + 22	6.37E + 21	1931 Main Crater wall; Half Cone agglutinate
NA92-59	56.8950	-158.1686	380±50	Qht	2/6	-	-	-	-	North base Vent Mountain; Half Cone agglutinate
NA02-10F	56.9015	-158.2244	380±50	Qht?	-/9	-	-	-	-	1931 Main Crater west wall; black agglutinate Half Cone?
NA02-11F	56.9066	-158.2132	>840±40	Qhc?	-/9	-	-	-	-	1931 Main Crater north wall; welded volcanoclastic
NA02-1B	56.8893	-158.1910	1931 CE	Q31t?	3/5	68.0	0.88	9.98E + 22	1.29E + 21	Between Blocky Cone and the base of Vent Mountain; 1931 scoria
NA97-10	56.9080	-158.2100	1931 CE	Q31l	2/5	-	-	-	-	1931 Main Crater floor near base of north wall; 1931 spatter-fed lava flow

Note. Lat and Lon are degrees latitude (north) and longitude (east) based on datum NAD83. Age is interpreted sample age (years before calendar year 1950 CE) and age uncertainty in years. *Unit* is the map unit from Figure 1. *m* is number of accepted specimens for successful samples, and *n* is total specimens measured. B_F is the estimated ancient field strength in microTesla (μ T), $B_F\sigma$ is the one standard deviation of B_F . VADM is the virtual axial dipole moment in ampere meter squared (A_m^2) and VADM σ is the one standard deviation of VADM. *Sample Location and Description* are descriptions of the field locality and physical sample.

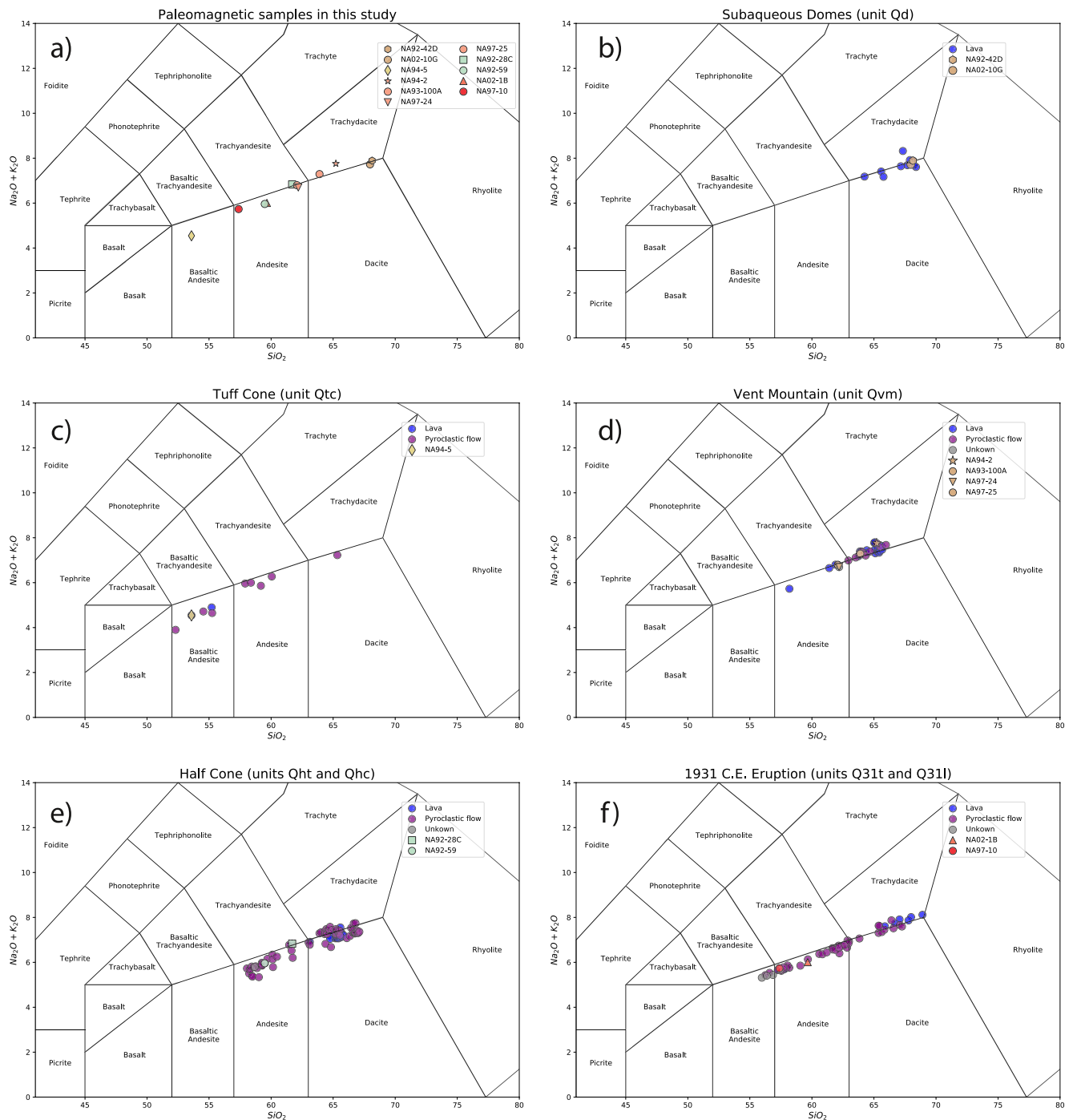


Figure 2. Total alkaline silica (TAS) plots for samples from post-Aniakchak II geologic units at Aniakhchak associated with this study. Plot (a) shows all samples used in this study with geochemical information. Plots (b–f) show samples for each geologic unit, including samples used in this study and other samples with geochemical information from Bacon et al. (2014). All geochemical information is from Appendix Table B1 in Bacon et al. (2014).

a minimum age constraint for the emplacement of the Tuff Cone unit. The tuff cones are thought to postdate catastrophic draining of the ancestral caldera lake ($1,860 \pm 30$ years BP; Bacon et al., 2014; VanderHoek & Myron 2004) to their approximate elevation in the caldera. This age is interpreted as a maximum age constraint for the emplacement of the Tuff Cone unit. We therefore assign an age range of sample NA94-5 to be between 900 and 1,860 years BP.

The geochemical composition of sample NA94-5 may further constrain its emplacement age. Sample NA94-5 was collected east of Windy Cone and has basaltic andesite geochemistry that resembles the mafic eruption material of the Tuff Cone unit (Figure 2). The range of total alkaline silicate (TAS) compositions for all Tuff Cone samples collected by Bacon et al. (2014) (Figure 2) indicates that there might have been a magmatic evolution of material from more felsic to more mafic compositions, perhaps similar to what was observed for the duration of the Aniakchak II caldera-forming eruption (Bacon et al., 2014). If magmatic evolution occurred during the development of the Tuff Cones, the low-silica/high-mafic composition of NA94-5 could indicate that it was emplaced near the end of the Tuff Cone eruptive period and could be closer to the younger radiocarbon age constraint of 900 ± 80 years BP (Bacon et al., 2014). However, without direct geochronologic constraints on the sample, we consider the age uncertainty of this sample to be 900–1,860 years BP.

3.1.3. Vent Mountain (Unit Qvm)

Samples NA97-25, NA94-2, NA97-24, and NA93-100A were collected from the Vent Mountain lava and scoria (unit Qvm; Figure 1) and were assigned ages of 400 ± 30 and 840–900 years BP (Table 1). The Vent Mountain scoria and spatter cone rises 440–530 m above the Aniakchak caldera floor and is the most prominent topographic feature within the caldera (Bacon et al., 2014). Lava flows and other eruptive materials of this unit were sourced from Vent Mountain itself, from fissures on the mountain flank, and from the nearby New Cone (Figure 1). Materials from Vent Mountain and New Cone are stratigraphically above the Tuff Cones unit (which has a minimum radiocarbon age of 900 ± 80 years BP; Bacon et al., 2014), below the 1931 CE. eruption, and are interbedded with eruptive materials from Half Cone (Bacon et al., 2014).

Samples NA94-2 and NA97-24 were collected from the rim of New Cone, and sample NA97-25 was described by Bacon et al. (2014) to have been sampled from a lava flow possibly related to New Cone (Table 1). Bacon et al. (2014) determined a radiocarbon mean age of 400 ± 30 years BP for tephra interpreted to have originated from New Cone based on multiple *ca.* 400 years BP radiocarbon ages of wood and organic sediments associated with these tephra deposits. We therefore assign this weighted radiocarbon mean age of 400 ± 30 years BP to samples NA94-2, NA97-24, and NA97-25.

Sample NA93-100A was reported to have been collected from a Vent Mountain “...lava younger than tuff cones, at base of tephra section” (Appendix Table B1 in Bacon et al. [2014]). We interpret this description to mean that the lava flow is the oldest Vent Mountain lava in the schematic composite stratigraphic section of Bacon et al. (2014) which has a minimum age of 840 ± 30 years BP and a maximum age of 900 ± 80 years BP. We therefore assign an age range of 840–900 years BP to sample NA93-100A.

3.1.4. Half Cone (Units Qht and Qhc)

Samples NA92-59, NA92-28C, and NA02-10F were collected from the Half Cone tephra (unit Qht; Figure 1), and sample NA02-11F was collected from the Half Cone Cobweb lava (unit Qhc). These samples were assigned ages of 380 ± 50 and $>840 \pm 40$ years BP (Table 1). Unit assignments for NA02-10F and NA02-11F were interpreted for this study based on their location information and descriptions (Table 1). These samples were not included in the chemical analysis of Aniakchak volcano by Bacon et al. (2014). Half Cone today is a remnant of an andesite–dacite composite edifice whose southeastern part had been destroyed by explosive eruptions late in its eruptive life. Volcanic materials from Half Cone generally consist of pumice-fall deposits, pyroclastic-flow deposits, tephra deposits, and dacitic lava flows. Materials from Half Cone are generally interbedded with those from Vent Mountain. Radiocarbon age dates of organic materials associated with Half Cone deposits range from 380 ± 50 to 840 ± 40 years BP (Bacon et al., 2014). Late eruption fall deposits and the Cobweb lava flow (the final eruptive product of Half Cone) are stratigraphically above the dated material and postdate those eruptive events.

Sample NA92-59 is from agglutinate material sampled at the north base of Vent Mountain. This sample is described to be from a late-erupted Half Cone pyroclastic fall layer stratigraphically above the Brown Pumice fall and the underlying Pink Pumice fall (380 ± 50 years BP radiocarbon age; Bacon et al. (2014)). The Brown Pumice Fall and Pink Pumice Fall were emplaced by a series of Plinian eruptions that produced widespread pumice falls and destroyed much of the original Half Cone edifice (Bacon et al., 2014). Sample NA92-59 has a SiO_2 weight percent of 59.49, which is within the reported range of the Brown Pumice fall of about 58–61 weight

percent (Bacon et al., 2014). The geochemistry data is consistent with the stratigraphic interpretation that this sample is related to the eruptive materials of the Half Cone pumice falls, we therefore assign the Pink Pumice Fall radiocarbon age of 380 ± 50 years BP to this sample.

Sample NA92-28C is agglutinate material sampled from the 1931 main crater wall (Table 1). Based on the sample descriptions and location of this sample, it is likely that sample NA92-28C was collected from the *ca.* 400 years BP. Half Cone agglutinate exposed in the north wall of the 1931 Main Crater (Bacon et al., 2014). Sample NA02-10F has a similar sample description and location as sample NA92-28C. Therefore, we interpret that sample NA02-10F was collected from the same agglutinate exposure. We assume that the *ca.* 400 years BP age ascribed by Bacon et al. (2014) for this exposure is derived from the 380 ± 50 years BP radiocarbon age for the Half Cone Pink Pumice Fall which is one of the most areally extensive units of Half Cone *ca.* 400 years BP Plinian eruptions. We therefore assign an age of 380 ± 50 years BP to both samples NA92-28C and NA02-10F.

Sample NA02-11F consists of welded volcanoclastic material collected from the north wall of the 1931 Main Crater. The welded agglutinate description for this sample is consistent with what Bacon et al. (2014) describes as partly welded or indurated coarse pyroclastic-flow material at the base of the 1931 Main Crater exposure. We interpret that sample NA02-11F was collected from this basal material. The basal unit is stratigraphically overlain by pumice-fall deposits in the 1931 Main Crater exposure, which Bacon et al. (2014) indicate may be correlative with the lower and upper light pumice that have weighted mean radiocarbon ages of 840 ± 40 and 570 ± 40 years BP, respectively. Based on the above interpretations, sample NA02-11F is likely older than the lower light pumice and we therefore assign an age of $>840 \pm 40$ years BP to the sample (Table 1).

3.1.5. 1931 CE Eruption (units Q31t and Q31l)

Samples NA02-1B and NA97-10 were collected from material emplaced during the 1931 CE eruption. Sample NA02-1B is a scoriaceous material from the 1931 Tephra (unit Q3t), and sample NA02-1B is from a spatter-fed lava flow from the 1931 Lava (unit Q3l). The 1931 CE. Aniakchak eruption was a 6-week-long eruption that began with relatively silica-rich dacite–rhyodacite magma and ended with relatively silica-poor basaltic andesite magma (Nicholson et al., 2011). Within and near the caldera, the 1931 deposit consists of pumiceous fall deposits (Nicholson et al., 2011). A 50–100-cm-thick stratified deposit of agglutinated basaltic-andesite lapilli and minor scoria bomb partly mantles the north and east wall of the Main Crater (Bacon et al., 2014). A vesicular basaltic andesite lava covers much of the floor of the Main Crater and is mantled by spatter agglutinate.

4. Methods

4.1. Paleointensity Experiment

Specimens were selected based on their visual and textural appearance for the paleointensity experiment (Figure 3). The glassy textures shown in all specimens in Figure 3 here are indicative of rapid cooling, which tends to promote the formation of single domain magnetic carriers that often succeed in paleointensity experiments (Tauxe & Staudigel, 2004). Specimens chosen for the paleointensity experiment have glassy textures and have a minimum magnetic moment of $1.0E^{-7}$ ampere meter squared (Am^2). Specimens were wrapped in non-magnetic glass microfiber filters and glued inside 12 mm-diameter glass vials with potassium silicate. All glass vials were treated with a 600°C heating in a zero-field to remove any remanent magnetization; vials used in the paleointensity experiment had a resulting magnetic moments smaller than $1.0E^{-10}\text{Am}^2$. Between five and nine specimens were prepared for each sample (Table 1).

Paleointensity experiments were conducted at the paleomagnetic laboratory at Scripps Institution of Oceanography at the University of California San Diego. All experiments were conducted in a shielded room which had a background magnetic field less than 400 nanoTesla (nT). The IZZI-modified double heating protocol was used for the paleointensity experiment (Yu et al., 2004) using custom-built ovens. For zero-field heating steps the background magnetic field in the ovens was reduced to less than 5 nT. A laboratory field of 35 microTesla (μT) was applied during in-field heating steps along the Z-axis of the oven, parallel to the long axis of glass vials. Specimens were treated up to 600°C or until at least 95% of the natural remanent magnetization (NRM) was removed. Partial thermal remanent magnetization (pTRM) checks for alterations were applied at every other temperature step. NRM and pTRM measurements were performed using a 2G Cryogenic Magnetometer.

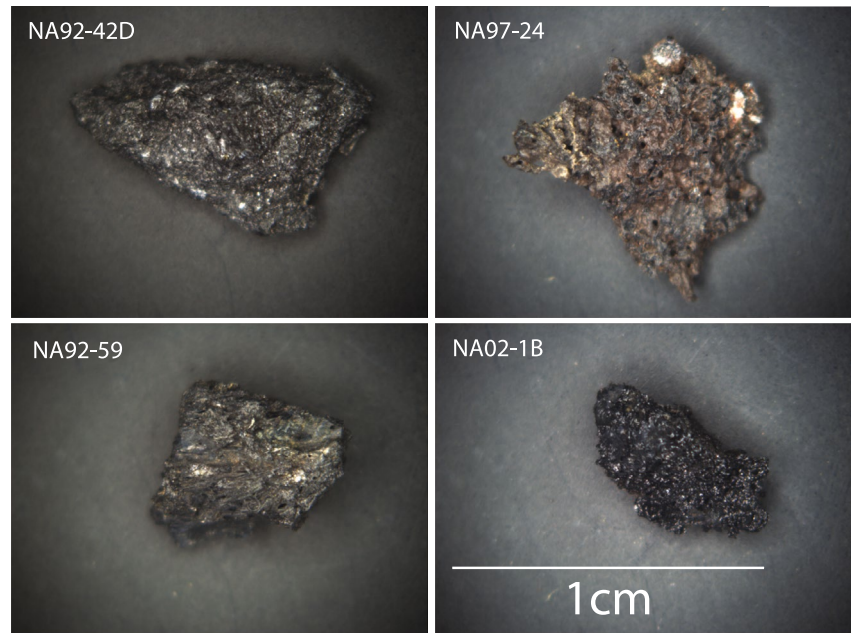


Figure 3. Binocular images of representative glassy volcanic materials that are sister specimens with those used for paleointensity experiments in this study. All images share the same scale as shown by the 1-cm scale bar in the image for sample NA02-1B.

4.2. Selection Criteria

Data interpretation was performed using the Thellier GUI Auto Interpreter (Shaar & Tauxe, 2013), part of the PmagPy software package (Tauxe et al., 2016), using the CCRIT selection criteria (Cromwell, Tauxe, Staudigel, & Ron, 2015). CCRIT was designed to limit the selected specimen results to be those containing only a single directional magnetic component and near-linear slopes in NRM/TRM Arai plots (Nagata, 1963). This criteria has been useful in filtering out non-ideal specimens, such as those with poor Arai behavior and those producing poor within-sample paleointensity dispersion. Specimen- and sample-level requirements of CCRIT are listed in Table 2, and brief descriptions are provided below (more detailed explanations of each criterium are presented in Paterson et al. [2014]). β is the standard deviation of the slope of selected data points normalized by the absolute value of the slope. SCAT is a Boolean based on the value of β and evaluates the degree of scatter of the selected data points about the best fit slope. Here the threshold of β is set at 0.1. FRAC measures the fraction of the NRM used in calculating the best fit line. Gap Max sets the maximum gap between two consecutive NRM/TRM points on Arai plot. MAD is the maximum angle of deviation representing the scatter of selected through demagnetization procedures about the unanchored best fit line. DANG measures the angle between the best fit line and the line determined by the center of mass of the selected data points and the origin. $|\vec{k}|$ is the absolute value of the degree of curvature of selected data points on Arai plots, put forward by Paterson (2011). A larger value of $|\vec{k}|$ indicates a more curved Arai plot. N is the minimum number of accepted specimens to calculate the sample-mean intensity. B_σ is the maximum accepted one-sigma standard deviation of sample-mean intensity, and

Table 2

Specimen- and Sample-Level Criteria for the CCRIT (Cromwell, Tauxe, & Halldórsson, 2015) Selection Method (SCAT Criterion Uses a $B_{\text{threshold}}$ Value of 0.1)

CCRIT paleointensity selection criteria							Sample		
Specimen									
SCAT	FRAC	Gap Max	β	MAD _{free}	DANG	$ \vec{k} $	N	B_σ	$B_\sigma\%$
PASS	≥ 0.78	≤ 0.60	≤ 0.10	$\leq 5.0^\circ$	$\leq 10.0^\circ$	≤ 0.164	≥ 3	$\leq 4 \mu\text{T}$	$\leq 10\%$

Note. Refer to the “Selection Criteria” section or Paterson et al. (2014) for descriptions of each statistic.

$B_o\%$ is the maximum accepted percentage of B_o relative to the sample-mean intensity; successful samples may not exceed both B_o and $B_o\%$.

5. Results and Discussion

A total of 36 out of 89 specimens passed the specimen-level CCRIT selection criteria. Six out of 13 samples passed the sample-level selection criteria and yielded high-quality absolute paleointensity results. Estimated paleointensity results from all accepted samples are listed in Table 1 and plotted as black symbols in Figure 5. Specimen-level paleointensity estimates and statistics for accepted samples are listed in Table 3. All sample- and specimen-level experimental results are archived in the MagIC database at <https://earthref.org/MagIC/19326> (Cromwell & Zhang, 2021). Successful samples have a mean paleointensity value of 58.8 μT with a standard deviation of 5.6 μT , which corresponds to a mean virtual axial dipole moment (VADM) of $86.3 \times 10^{21} \text{ Am}^2$ (ZAm^2) with a standard deviation of 4.93 ZAm^2 . The range of paleointensity values for the successful samples ranged from 49.5 to 68.0 μT , corresponding to VADM values that range from 63.7 to 99.8 ZAm^2 (Figure 5).

Representative specimen results from the IZZI paleointensity experiment are shown in Figure 4 as NRM/TRM paleointensity plots and orthogonal demagnetization plots. Specimens in samples that passed CCRIT exhibit linear ratios between TRM acquired during in-field steps and NRM lost during associated zero-field steps, with reproducible pTRM checks (Figure 4). Specimens from the same sample that pass the paleointensity result selection generally have consistent behaviors, likely associated with their close mineralogy assemblages. The majority of accepted specimens show single-component orthogonal demagnetization plots (Figure 4), consistent with the interpretation that they have retained primary NRMs during cooling after eruption and have acquired minimum secondary overprints.

Specimens that did not pass CCRIT (Figure 4) selection were rejected for displaying non-linear TRM/NRM behavior over the course of the heating experiment. For example, specimen NA02-11Fi and NA92-59e (Figure 4) exhibit zigzagging and sagging Arai plot with failed pTRM checks beginning at 300°C and 510°C, respectively. This is likely due to the contribution of vortex state or multi-domain (MD) magnetic grains within the specimens. Because vortex state and MD grains often unblock differently between in-field and zero-field steps (Tauxe & Staudigel, 2004; Yu et al., 2004), the alternating steps of in-field/zero-field (IZ) and zero-field/in-field (ZI) IZZI experimental protocol results in zigzagging or sagging of the Arai plot. Specimen NA97-25d has a linear Arai plot, but it fails the Gap Max criterion because of the great loss of NRM intensity between temperature steps 200°C and 300°C. In addition, the majority of the remanence in this specimen was removed after the 300°C heating step, indicating that the dominant magnetic carrier within the specimen is not likely stoichiometric single-domain magnetite and may be prone to secondary overprint.

Figure 5 summarizes individual specimen paleointensity results, sample-mean paleointensity results with one standard deviations, and locality-mean value of all successful samples (58.8 μT). Shown for comparison are the mean of the predicted surface intensities from global geomagnetic field model estimates at Aniakchak volcano for the last 2,500 years BP from models PFM9K.1b (Nilsson et al., 2014), CALS10k.2 (Constable et al., 2016), and HFMOL1.A1 (Constable et al., 2016). Specimens from samples that passed the CCRIT selection criteria generally yield consistent specimen-level paleointensity estimates. The overall sample-mean paleointensity estimates show a similar trend in field intensity as predicted by the geomagnetic field models, although the absolute paleointensity values of the samples tends to be lower than that of the models (Figure 5). The sample and model intensities follow a high-low-high trend from *ca.* 2,300 to the present; they tend to peak between about 1,600 and 2,000 years BP, decline to a low at about 1,300 years BP, and peak again between about 300 and 500 years BP.

The mean paleointensity estimate from sample NA92-42D which is from the subaqueous domes (unit Qd), is lower than the predicted values from the geomagnetic field models at *ca.* 2,100 years BP. However, given its estimated age range between 1,860 and 2,300 years BP, an interpretation could be allowed that this sample was emplaced close to 2,300 years BP during the widespread pumice fall that was synchronous with, or predates, the emplacement of the subaqueous domes (Bacon et al., 2014). If sample NA92-42D was emplaced close to 2,300 years BP, its paleointensity value would be consistent with those predicted by models CALS10k.2 and HFMOL1.A1 and nearly within uncertainty of model PFM9K.1b (Figure 5).

Sample NA94-5 from Tuff Cone (unit Qtc) has a mean paleointensity estimate lower than what is predicted by all three geomagnetic field models (Figure 5). This sample has a broad estimated age range between 900 and

Table 3
Summary Table of Specimen-Level Paleointensity Experiment Results

Specimen	Sample	B_F	T_{low}	T_{high}	n	n_{pTRM}	SCAT	FRAC	Gap Max	β	MAD_{free}	DANG	$ \bar{k} $
NA92-42Da	NA92-42D	58.76	0	400	6	2	PASS	0.92	0.46	0.08	3.60	1.56	-0.020
NA92-42Db	NA92-42D	58.16	100	400	5	2	PASS	0.88	0.52	0.06	2.02	2.37	-0.080
NA92-42Dc	NA92-42D	58.27	100	400	5	2	PASS	0.89	0.51	0.05	2.99	3.01	0.00
NA92-42Dd	NA92-42D	64.15	0	430	7	2	PASS	0.95	0.48	0.04	1.76	1.60	0.040
NA92-42De	NA92-42D	57.53	0	400	6	2	PASS	0.92	0.46	0.05	2.24	2.39	0.080
NA92-42Df	NA92-42D	48.62	100	460	7	3	PASS	0.92	0.55	0.04	3.92	2.37	-0.100
NA92-42Dg	NA92-42D	-	-	-	-	-	-	-	-	-	-	-	-
NA02-10Ga	NA02-10G	-	-	-	-	-	-	-	-	-	-	-	-
NA02-10Gb	NA02-10G	-	-	-	-	-	-	-	-	-	-	-	-
NA02-10Gc	NA02-10G	-	-	-	-	-	-	-	-	-	-	-	-
NA02-10Gd	NA02-10G	-	-	-	-	-	-	-	-	-	-	-	-
NA02-10Ge	NA02-10G	-	-	-	-	-	-	-	-	-	-	-	-
NA02-10Gf	NA02-10G	-	-	-	-	-	-	-	-	-	-	-	-
NA02-10Gg	NA02-10G	-	-	-	-	-	-	-	-	-	-	-	-
NA94-5a	NA94-5	-	-	-	-	-	-	-	-	-	-	-	-
NA94-5b	NA94-5	48.53	0	430	7	2	PASS	0.81	0.37	0.05	4.88	4.88	0.160
NA94-5c	NA94-5	46.57	0	430	7	2	PASS	0.79	0.34	0.06	3.56	1.39	0.000
NA94-5d	NA94-5	-	-	-	-	-	-	-	-	-	-	-	-
NA94-5e	NA94-5	-	-	-	-	-	-	-	-	-	-	-	-
NA94-5f	NA94-5	51.27	0	430	7	2	PASS	0.85	0.35	0.06	3.17	2.29	0.120
NA94-5g	NA94-5	-	-	-	-	-	-	-	-	-	-	-	-
NA94-5h	NA94-5	55.96	200	560	11	5	PASS	0.89	0.21	0.04	4.96	1.22	0.000
NA94-5i	NA94-5	44.93	200	580	12	6	PASS	0.84	0.14	0.04	2.86	0.97	-0.040
NA94-2a	NA94-2	55.59	100	460	7	3	PASS	0.95	0.59	0.02	1.86	0.81	0.000
NA94-2b	NA94-2	57.90	0	490	9	3	PASS	0.96	0.52	0.05	2.89	0.93	0.150
NA94-2c	NA94-2	59.40	0	510	10	4	PASS	0.99	0.54	0.03	1.54	0.79	0.160
NA94-2d	NA94-2	54.87	0	460	8	3	PASS	0.97	0.46	0.04	1.44	1.10	-0.040
NA94-2e	NA94-2	52.08	100	460	7	3	PASS	0.95	0.59	0.02	1.54	0.99	0.090
NA94-2f	NA94-2	62.41	0	490	9	3	PASS	0.98	0.57	0.03	1.73	0.80	-0.050
NA97-24a	NA97-24	58.84	350	580	10	6	PASS	0.82	0.28	0.03	3.80	0.26	0.000
NA97-24b	NA97-24	62.20	0	580	14	6	PASS	1	0.14	0.03	2.52	0.33	0.100
NA97-24c	NA97-24	-	-	-	-	-	-	-	-	-	-	-	-
NA97-24d	NA97-24	58.59	0	545	12	5	PASS	0.78	0.41	0.04	4.23	0.76	0.000
NA97-24e	NA97-24	57.99	200	545	10	5	PASS	0.79	0.31	0.03	4.15	2.43	0.000
NA97-24f	NA97-24	56.35	200	560	11	5	PASS	0.96	0.39	0.04	3.92	0.79	0.160
NA97-24g	NA97-24	58.72	0	545	12	5	PASS	0.88	0.38	0.03	3.45	1.80	0.000
NA97-25a	NA97-25	-	-	-	-	-	-	-	-	-	-	-	-
NA97-25b	NA97-25	-	-	-	-	-	-	-	-	-	-	-	-
NA97-25c	NA97-25	-	-	-	-	-	-	-	-	-	-	-	-
NA97-25d	NA97-25	-	-	-	-	-	-	-	-	-	-	-	-
NA97-25e	NA97-25	-	-	-	-	-	-	-	-	-	-	-	-
NA97-25f	NA97-25	-	-	-	-	-	-	-	-	-	-	-	-
NA93-100Aa	NA93-100A	-	-	-	-	-	-	-	-	-	-	-	-

Table 3
Continued

Specimen	Sample	B_F	T_{low}	T_{high}	n	n_{pTRM}	SCAT	FRAC	Gap Max	β	MAD_{free}	DANG	$ \bar{k} $
NA93-100Ab	NA93-100A	42.60	100	510	9	4	PASS	0.87	0.34	0.02	4.00	6.00	0.002
NA93-100Ac	NA93-100A	42.80	0	460	8	3	PASS	0.85	0.38	0.05	3.30	8.70	0.065
NA93-100Ad	NA93-100A	–	–	–	–	–	–	–	–	–	–	–	–
NA93-100Ae	NA93-100A	–	–	–	–	–	–	–	–	–	–	–	–
NA93-100Af	NA93-100A	–	–	–	–	–	–	–	–	–	–	–	–
NA93-100Ag	NA93-100A	–	–	–	–	–	–	–	–	–	–	–	–
NA92-28Ca	NA92-28C	59.60	0	530	11	4	PASS	0.81	0.19	0.02	1.82	0.96	–0.020
NA92-28Cb	NA92-28C	58.40	0	530	11	4	PASS	0.82	0.22	0.02	1.96	0.40	0.130
NA92-28Cc	NA92-28C	61.74	0	560	13	5	PASS	0.97	0.19	0.04	2.04	0.40	0.070
NA92-28Cd	NA92-28C	–	–	–	–	–	–	–	–	–	–	–	–
NA92-28Ce	NA92-28C	–	–	–	–	–	–	–	–	–	–	–	–
NA92-28Cf	NA92-28C	68.13	0	560	13	5	PASS	0.99	0.24	0.03	2.90	0.25	–0.160
NA92-59a	NA92-59	73.50	100	490	8	3	PASS	0.83	0.23	0.04	2.10	105.0	0.000
NA92-59b	NA92-59	–	–	–	–	–	–	–	–	–	–	–	–
NA92-59c	NA92-59	–	–	–	–	–	–	–	–	–	–	–	–
NA92-59d	NA92-59	–	–	–	–	–	–	–	–	–	–	–	–
NA92-59e	NA92-59	–	–	–	–	–	–	–	–	–	–	–	–
NA92-59f	NA92-59	73.60	0	460	8	3	PASS	0.83	0.23	0.03	2.40	1.10	–0.141
NA02-10Fa	NA02-10F	–	–	–	–	–	–	–	–	–	–	–	–
NA02-10Fb	NA02-10F	–	–	–	–	–	–	–	–	–	–	–	–
NA02-10Fc	NA02-10F	–	–	–	–	–	–	–	–	–	–	–	–
NA02-10Fd	NA02-10F	–	–	–	–	–	–	–	–	–	–	–	–
NA02-10Fe	NA02-10F	–	–	–	–	–	–	–	–	–	–	–	–
NA02-10Ff	NA02-10F	–	–	–	–	–	–	–	–	–	–	–	–
NA02-10Fg	NA02-10F	–	–	–	–	–	–	–	–	–	–	–	–
NA02-10Fh	NA02-10F	–	–	–	–	–	–	–	–	–	–	–	–
NA02-10Fi	NA02-10F	–	–	–	–	–	–	–	–	–	–	–	–
NA02-11Fa	NA02-11F	–	–	–	–	–	–	–	–	–	–	–	–
NA02-11Fb	NA02-11F	–	–	–	–	–	–	–	–	–	–	–	–
NA02-11Fc	NA02-11F	–	–	–	–	–	–	–	–	–	–	–	–
NA02-11Fd	NA02-11F	–	–	–	–	–	–	–	–	–	–	–	–
NA02-11Fe	NA02-11F	–	–	–	–	–	–	–	–	–	–	–	–
NA02-11Ff	NA02-11F	–	–	–	–	–	–	–	–	–	–	–	–
NA02-11Fg	NA02-11F	–	–	–	–	–	–	–	–	–	–	–	–
NA02-11Fh	NA02-11F	–	–	–	–	–	–	–	–	–	–	–	–
NA02-11Fi	NA02-11F	–	–	–	–	–	–	–	–	–	–	–	–
NA02-1Ba	NA02-1B	67.73	0	570	14	6	PASS	0.93	0.32	0.02	2.63	1.71	0.000
NA02-1Bb	NA02-1B	68.95	200	560	11	5	PASS	0.83	0.36	0.05	2.73	0.61	–0.030
NA02-1Bc	NA02-1B	67.25	0	560	13	5	PASS	0.80	0.18	0.03	3.79	2.64	0.000
NA02-1Bd	NA02-1B	–	–	–	–	–	–	–	–	–	–	–	–
NA02-1Be	NA02-1B	–	–	–	–	–	–	–	–	–	–	–	–
NA97-10a	NA97-10	–	–	–	–	–	–	–	–	–	–	–	–
NA97-10b	NA97-10	–	–	–	–	–	–	–	–	–	–	–	–

Table 3
Continued

Specimen	Sample	B_F	T_{low}	T_{high}	n	n_{pTRM}	SCAT	FRAC	Gap Max	β	MAD_{free}	DANG	$ \bar{k} $
NA97-10c	NA97-10	38.70	100	490	8	3	PASS	0.81	0.32	0.02	3.20	5.30	-0.003
NA97-10d	NA97-10	-	-	-	-	-	-	-	-	-	-	-	-
NA97-10e	NA97-10	49.10	0	430	7	2	PASS	0.81	0.36	0.02	2.40	1.20	-0.134

Note. Paleointensity results and selection criteria statistics are listed for specimens that passed the CCRIT selection criteria. Specimen and Sample are paleomagnetic specimens and their respective samples. B_F is the measured intensity in microTesla, T_{low} and T_{high} are lower and upper temperature bounds ($^{\circ}\text{C}$) used to calculate intensity, and n and n_{pTRM} are the number of temperature steps and pTRM checks used in that same calculation. SCAT, FRAC, Gap Max, β , MAD_{free} , DANG, and $|\bar{k}|$ are statistics used to determine specimen reliability. See "Selection Criteria" section for a description of all statistics, and Table 2 for selection criteria.

1,860 years BP. If the age of this sample is closer to the minimum age estimate (as may be indicated by geochemical data, see "Stratigraphy and Age Constraints" section) then the range of paleointensity values of sample NA94-5 could be more consistent with the relatively low intensity values predicted by the three geomagnetic field models at about 1,100 years BP. If this was the case, the paleointensity of sample NA94-5 would be consistent with the predicted decreasing trend in geomagnetic field intensity at Aniakchak volcano since the high between about 1,600 and 2,000 years BP, although the estimated absolute field intensity would underestimate that predicted by the field models.

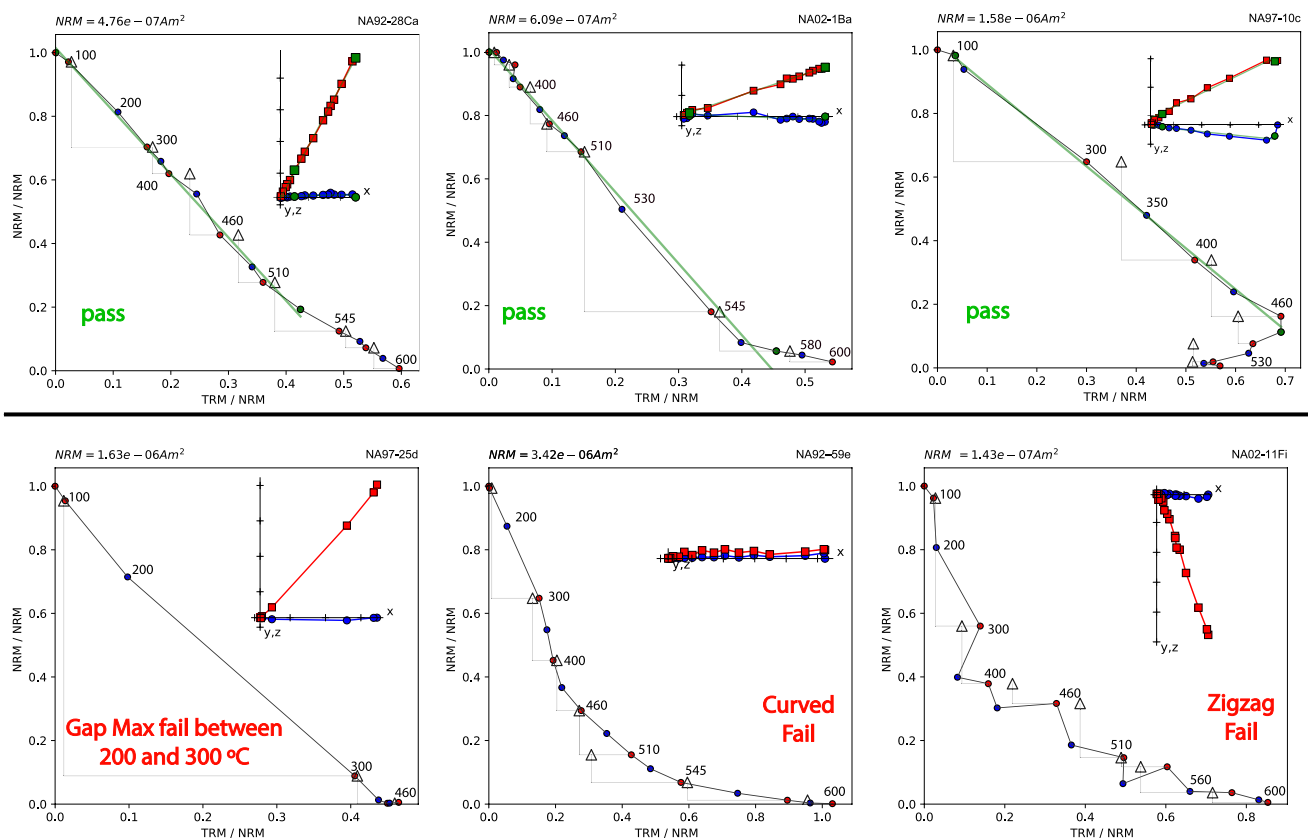


Figure 4. Representative specimen paleointensity Arai plots, showing normalized thermal remanent magnetization acquired during in-field heating steps plotted against normalized natural remanent magnetization removed during zero-field steps. In the Arai plots, temperature values are listed in degree Celsius, pTRM checks are shown as triangles, zero-field/in-field temperature steps are shown as red dots, in-field/zero-field steps are shown in blue. The green line is the least squares component fit for selected temperature steps for specimens that pass the selection criteria. Inset orthogonal vector demagnetization diagrams (in specimen coordinates) show that the specimens have dominantly single component remanent magnetizations. Figures in the top row show typical paleointensity behavior of specimens with dominantly straight slope of NRM/TRM that pass the CCRIT selection criteria (Cromwell, Tauxe, Staudigel, & Ron, 2015); the bottom row shows typical behavior of specimens that fail the selection criteria.

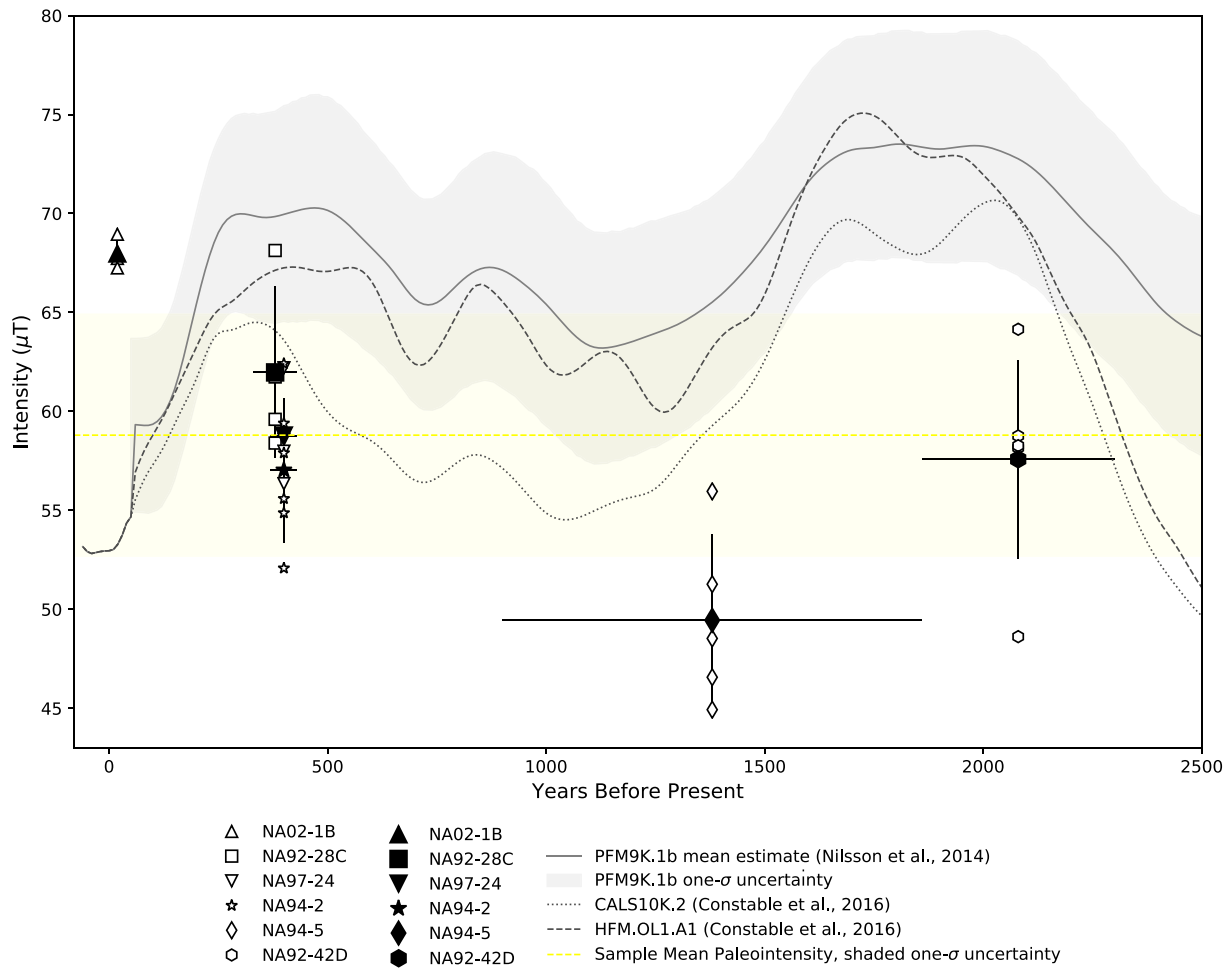


Figure 5. Absolute paleointensity results of samples that passed the CCRIT selection criteria from Aniakchak volcano with respect to predicted paleointensity values at Aniakchak volcano from global geomagnetic field models PFM9K.1b (Nilsson et al., 2014), CALS10k.2 (Constable et al., 2016), and HFM.OL1.A1 (Constable et al., 2016). The one standard deviation (1σ) uncertainty for model PFM9K.1b is shown as the gray area. Individual specimen paleointensity estimates (open symbols), sample-level mean paleointensity results (closed symbols), together with 1σ uncertainties are plotted with respect to their estimated ages with uncertainties (Table 1). Dashed yellow line and yellow rectangular area represents the mean paleointensity value of all samples (58.8 microTesla) and 1σ uncertainty. 1950 CE is used as zero years before present.

Samples NA94-2 and NA97-24 from Vent Mountain (unit Qvm), and sample NA92-28C from Half Cone (unit Qht) have similar estimated ages of 400 ± 30 and 380 ± 50 years BP, respectively, and have indistinguishable estimated paleointensity values within the calculated uncertainty (Table 1; Figure 5). Despite having equivalent paleointensity estimates, the mean value of the individual samples vary with respect to the predicted intensity of the geomagnetic field models. Samples NA94-2 and NA97-24 have lower estimated intensities than all three field models, while the uncertainty bounds of sample NA92-28C are consistent with model CALS10k.2 and within the uncertainty of model PFM9K.1b. The paleointensity of samples NA94-2, NA97-24, and NA92-28C follow the predicted increasing trend in geomagnetic field intensity at Aniakchak volcano since about 1,100 years BP, although the absolute field intensity values from the samples are generally lower than those predicted by the field models.

Sample NA02-1B from the 1931 CE tephra (unit Q3t) has a mean paleointensity estimate of $68.0 \mu\text{T}$, about $15 \mu\text{T}$ (25%) higher than the historical field strength at Aniakchak volcano in 1931 CE ($53.2 \mu\text{T}$; estimated from IGRF12 using *igrf.py*, included as part of the *PmagPy* software package [Tauxe et al., 2016]) and greater than the predicted intensity from the geomagnetic field models (Table 1; Figure 5). The substantial overestimate of the historical field strength warrants additional consideration of the experimental results for sample NA01-1B together with sample NA97-10, which was also emplaced during the 1931 CE eruption (part of the 1931 CE lava

Table 4
Summary Table of Estimated Paleointensity Results of the 1931 CE Eruption From the Bias Corrected Estimation of Paleointensity (BiCEP) Method (Cych et al., 2021)

Specimen	Sample	B_F	B_F -Min	B_F -Max	T_{low}	T_{high}	\bar{k}	\bar{k} -Min	\bar{k} -Max
NA02-1Ba	NA02-1B	65.4	62.3	69.1	0	570	0.157	0.002	0.309
NA02-1Bb	NA02-1B	67.8	59.1	81.0	200	560	0.021	-0.389	0.421
NA02-1Bc	NA02-1B	65.4	60.6	71.3	0	560	0.100	-0.122	0.317
NA02-1Bd	NA02-1B	67.9	62.8	73.8	200	560	0.190	-0.058	0.429
NA02-1Be	NA02-1B	63.8	55.2	77.2	100	560	0.098	-0.298	0.477
NA97-10a	NA97-10	44.5	34.6	52.1	300	490	0.304	-0.244	0.719
NA97-10b	NA97-10	57.6	51.5	63.0	300	570	0.153	-0.148	0.453
NA97-10c	NA97-10	38.9	36.6	42.1	100	490	0.003	-0.199	0.225
NA97-10d	NA97-10	47.1	37.9	57.8	300	460	0.704	-0.658	1.424
NA97-10e	NA97-10	48.5	45.8	51.9	0	430	-0.130	-0.298	0.079
	1931 CE	57.8	52.7	62.3					

Note. Specimen and Sample are paleomagnetic specimens and their respective samples. B_F is the estimated intensity in microTesla, B_F -Min and B_F -Max are 95% confidence interval minimum and maximum estimates of paleointensity. T_{low} and T_{high} are lower and upper temperature bounds (°C) used in the BiCEP estimation. \bar{k} -Min and \bar{k} -Max are the minimum and maximum range estimates of the \bar{k} statistic. The resulting paleointensity estimate for the 1931 CE eruption from all specimens is listed with the one-sigma uncertainty range. Bolded values are the resulting BiCEP estimation of the 1931 CE eruption for all specimens from samples NA02-1B and NA97-10.

flow unit, Q31). Arai plots of specimens from sample NA02-1B show hints of double-slope behavior that could be the result of unrecognized thermochemical alterations or post-emplacement heating, which could reduce the accuracy of the paleointensity interpretations from specimens that pass CCRIT (top left plot in Figure 4; Bowles et al., 2015). The double-slope behaviors in these specimens include a low temperature component between 0–300°C and a higher temperature component between 350–560°C. After 560°C the specimens show signs of alteration as evidenced by failed pTRM checks (Figure 4). These specimens pass the CCRIT selection criteria despite observed non-linearity in the Arai plots, and yield consistent inter-sample paleointensity results (Figure 4; Tables 1 and 3). Nevertheless, the possibility remains that the presence of MD grains or post-emplacement alterations could have led to erroneous paleointensity estimates.

Two specimens from sample NA97-10 pass the specimen-level CCRIT selection criteria and have estimated paleointensity values of 38.7 μ T and 49.1 μ T (Tables 1 and 3). However, sample NA97-10 failed the CCRIT sample-level criteria because a minimum of three specimens is required. The two successful specimens have linear Arai plots up to 406°C, after which they show signs of alteration as evidenced by failed pTRM checks (top right plot in Figure 4). Like the specimens from NA02-1B, the Arai plots of specimens from NA97-10 show hints of double-slope behavior at lower temperatures, as well as directional overprints in the Zijdeveld diagrams. The successful specimen intensity values are about 4–15 μ T lower than the historical field strength at Aniakhchak volcano (53.2 μ T) and at least 19 μ T lower than the mean intensity for sample NA02-1B (68.0 μ T). If the successful specimens from both 1931 CE samples were combined, the resulting mean paleointensity would be 58.3 ± 13.7 μ T and would have encompassed the historical field strength, although the resulting estimate would have failed the CCRIT B_o and $B_o\%$ sample-level criteria.

We apply the Bias Corrected Estimation of Paleointensity (BiCEP) method of Cych et al. (2021) as a different means of estimating the paleointensity and uncertainty from the 1931 CE samples. BiCEP is a Bayesian method which accounts for bias in paleointensity estimates of specimens, effectively weighting the paleointensity of different specimens using the curvature of the Arai plot as a metric of nonlinearity (where linearity is measured by the \bar{k} statistic) and a predictor of bias (Cych et al., 2021). Specimen paleointensity and bias are estimated using a range of selected temperature steps in the Arai plot. For the BiCEP calculation, we provided temperature steps for all specimens from samples NA02-1B and NA97-10, including those that failed the CCRIT selection criteria (Table 4). For the specimens that passed CCRIT, we used the temperature steps from the Thellier-GUI

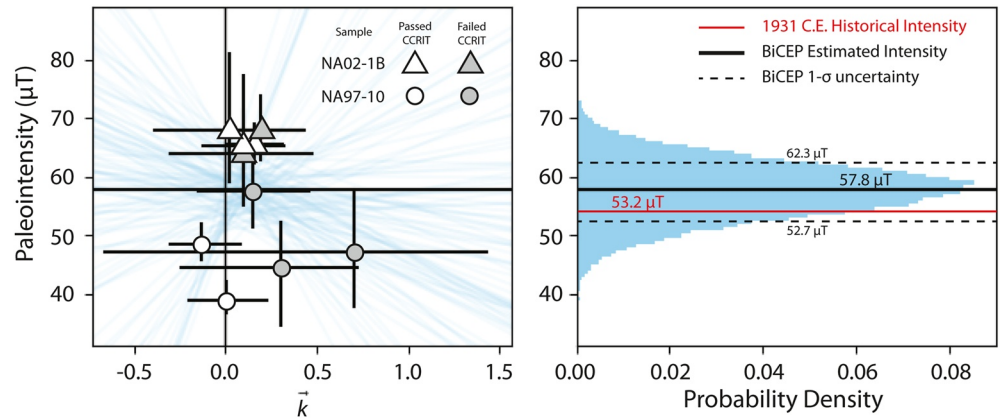


Figure 6. Estimated paleointensity results of the 1931 CE eruption from the Bias Corrected Estimation of Paleointensity (BiCEP) method (Cych et al., 2021). Left plot, estimated range of individual specimen paleointensity estimates relative to the estimated \bar{k} ; right plot, resulting estimate of 1931 CE field intensity and probability distribution.

estimation (Table 3). For the specimens that failed CCRIT we provided the temperature steps that represented the characteristic NRM/TRM of the paleointensity experiment, excluding low-temperature steps that deviate from the characteristic remanent magnetization direction on the Zijderveld plots, and high-temperature steps where thermochemical alteration occurred as evidenced by failed pTRM checks in the Arai plot.

The BiCEP estimation using all specimens from samples NA02-1B and NA97-10 generated “B-Grade” results (Cych et al., 2021), which are shown in Figure 6. The range of individual specimen paleointensity estimates relative to the range of estimated \bar{k} is shown on the left plot of Figure 6. The distribution and range of estimates on the plot is typical to the BiCEP calculation when the specimen-level experimental results have a range of quality and linearity in their Arai plot. The resulting probability distribution of estimated paleointensities is shown on the right plot of Figure 6. The median paleointensity value from the probability distribution was 57.8 μT , about 4.5 μT higher than the 1931 CE historical field intensity (Figure 6). The calculated 1σ uncertainty range from BiCEP was 52.7 μT and 62.3 μT . The resulting paleointensity estimate from BiCEP is within the 1σ uncertainty range of the historical field strength for 1931 CE. The BiCEP method provides a reasonable estimate and associated uncertainty of the 1931 CE field intensity at Aniakchak volcano based on the experimental results from the available samples. The inter-sample variability between the 1931 CE samples indicates that there may be rock magnetic, mineralogical, and (or) post-emplacement effects that affected the viability of the paleointensity experiment, warranting further investigation of these samples and additional sample collection.

6. Conclusion

In this study we report high-quality paleointensity results for the past 2,300 years from rapidly cooled, glassy volcanic material from Aniakchak volcano, Alaska, USA. Six samples pass the CCRIT selection criteria and provide paleointensity estimates. These new paleointensity results are a valuable contribution to the mid- to high-northern latitude paleomagnetic data set for North America. Although our sample-mean paleointensities are generally lower than predicted model intensities, paleointensity results for five samples are generally consistent with predicted variability in field strengths from global geomagnetic field models, considering age and experimental uncertainties. One sample for the historical 1931 CE eruption passed the CCRIT selection criteria and had robust inter-specimen consistency. However it yielded a paleointensity result about 15 μT higher than the historical field strength. Further analyses using a Bayesian estimation method of specimens from this sample and another sample from the 1931 CE eruption yielded a probability estimate with 1σ uncertainty that is consistent with the historical field strength. Further investigation of samples from the 1931 CE eruption is warranted to investigate potential rock magnetic, mineralogical, and (or) post-emplacement effects on the paleointensity results. Overall, the paleointensity results from Aniakchak volcano help provide new spatial and temporal coverage for future geomagnetic field models. Additional sampling of glassy volcanic materials paired with more precise age controls in future studies at Aniakchak volcano and other volcanoes along the Alaska-Aleutian arc will further constrain estimates of geomagnetic field behavior in North America.

Data Availability Statement

All measurement-level data and results are archived in the MagIC database and can be accessed at <https://earthref.org/MagIC/19326> and <https://dx.doi.org/10.7288/V4/MAGIC/19326>. Python scripts used to extract data from the PmagPy software package, analyze paleointensity data from Aniakchak volcano, and generate selected figures are archived at <http://earthref.org/ERDA/2502>. Support was provided through National Science Foundation grant EAR1520788 to G. Cromwell.

Acknowledgments

The authors thank Scott Bogue for his support throughout this grant. The authors thank Michelle Coombs and the staff at the USGS Alaska Volcano Observatory and the Geologic Materials Center in Anchorage, Alaska for providing access to sample material. Thanks to Jordan Brethauer and Cole Valentino for their work in collecting sample material from the Alaska Volcano Observatory archives. We thank Brendan Cych for help with the BiCEP result interpretations. The authors also thank two anonymous reviewers for their constructive reviews, and the editorial staff at the journal. Support was provided through National Science Foundation grant EAR1520788 to G. Cromwell.

References

- Bacon, C. R., Neal, C. A., Miller, T. P., McGimsey, R. G., & Nye, C. J. (2014). Postglacial eruptive history, geochemistry, and recent seismicity of Aniakchak volcano, Alaska Peninsula (*US Geological Survey Professional Paper* 1810, p. 74). <https://doi.org/10.3133/pp1810>
- Barletta, F., St-Onge, G., Channell, J. E., Rochon, A., Polyak, L., & Darby, D. (2008). High-resolution paleomagnetic secular variation and relative paleointensity records from the western Canadian Arctic: Implication for Holocene stratigraphy and geomagnetic field behaviour. *Canadian Journal of Earth Sciences*, 45(11), 1265–1281. This article is one of a series of papers published in this Special Issue on the theme Polar Climate Stability Network. GEOTOP Contribution 2008-0024. <https://doi.org/10.1139/e08-039>
- Begét, J., Mason, O., & Anderson, P. (1992). Age, extent and climatic significance of the c. 3400 BP Aniakchak tephra, western Alaska, USA. *The Holocene*, 2(1), 51–56. <https://doi.org/10.1177/095968369200200106>
- Bingham, D. K., & Stone, D. B. (1972). Palaeosecular variation of the geomagnetic field in the Aleutian Islands, Alaska. *Geophysical Journal International*, 28(4), 317–335. <https://doi.org/10.1111/j.1365-246x.1972.tb06796.x>
- Bowles, J. A., Gee, J. S., Jackson, M. J., & Avery, M. S. (2015). Geomagnetic paleointensity in historical pyroclastic density currents: Testing the effects of emplacement temperature and postemplacement alteration. *Geochemistry, Geophysics, Geosystems*, 16(10), 3607–3625. <https://doi.org/10.1002/2015gc005910>
- Brown, M. C., Donadini, F., Korte, M., Nilsson, A., Korhonen, K., Lodge, A., et al. (2015). GEOMAGIA50.v3: 1. General structure and modifications to the archeological and volcanic database. *Earth, Planets and Space*, 67(1). <https://doi.org/10.1186/s40623-015-0232-0>
- Brown, M. C., Donadini, F., Nilsson, A., Panovska, S., Frank, U., Korhonen, K., et al. (2015). GEOMAGIA50.v3: 2. A new paleomagnetic database for lake and marine sediments. *Earth, Planets and Space*, 67(1). <https://doi.org/10.1186/s40623-015-0233-z>
- Cai, S., Tauxe, L., & Cromwell, G. (2017). Paleointensity from subaerial basaltic glasses from the Second Hawaii Scientific Drilling Project (HSDP2) core and implications for possible bias in data from lava flow interiors. *Journal of Geophysical Research: Solid Earth*, 122(11), 8664–8674. <https://doi.org/10.1002/2017jb014683>
- Coe, R. S. (1967). The determination of paleo-intensities of the Earth's magnetic field with emphasis on mechanisms which could cause non-ideal behavior in Thellier's method. *Journal of Geomagnetism and Geoelectricity*, 19(3), 157–179. <https://doi.org/10.5636/jgg.19.157>
- Coe, R. S., Zhao, X., Lyons, J. J., Pluhar, C. J., & Mankinen, E. A. (2000). Revisiting the 1964 collection of Nunivak lava flows. *Eos, Transactions American Geophysical Union*, 81(48). Fall Meeting Suppl., Abstract GP62A-06.
- Constable, C., Korte, M., & Panovska, S. (2016). Persistent high paleosecular variation activity in southern hemisphere for at least 10000 years. *Earth and Planetary Science Letters*, 453, 78–86. <https://doi.org/10.1016/j.epsl.2016.08.015>
- Cromwell, G., Tauxe, L., & Halldórsson, S. A. (2015). New paleointensity results from rapidly cooled Icelandic lavas: Implications for Arctic geomagnetic field strength. *Journal of Geophysical Research: Solid Earth*, 120(5), 2913–2934. <https://doi.org/10.1002/2014jb011828>
- Cromwell, G., Tauxe, L., Staudigel, H., & Ron, H. (2015). Paleointensity estimates from historic and modern Hawaiian lava flows using glassy basalt as a primary source material. *Physics of the Earth and Planetary Interiors*, 241, 44–56. <https://doi.org/10.1016/j.pepi.2014.12.007>
- Cromwell, G., Trusdell, F., Tauxe, L., Staudigel, H., & Ron, H. (2018). Holocene paleointensity of the Island of Hawai'i from glassy volcanics. *Geochemistry, Geophysics, Geosystems*, 19(9), 3224–3245. <https://doi.org/10.1002/2017gc006927>
- Cromwell, G., & Zhang, Y. (2021). Archive of paleointensity data from Aniakchak Volcano, Alaska. Magnetics Information Consortium (Mag-IC). <https://doi.org/10.7288/V4/MAGIC/19326>
- Cych, B., Morzfeld, M., & Tauxe, L. (2021). Bias corrected estimation of paleointensity (BiCEP): An improved methodology for obtaining paleointensity estimates. *Geochemistry, Geophysics, Geosystems*, 22(8). <https://doi.org/10.1029/2021gc009755>
- Dreher, S. T., Eichelberger, J. C., & Larsen, J. F. (2005). The petrology and geochemistry of the Aniakchak caldera-forming ignimbrite, Aleutian Arc, Alaska. *Journal of Petrology*, 46(9), 1747–1768. <https://doi.org/10.1093/petrology/egi032>
- Dunlop, D. J. (2005). Linear and nonlinear Thellier paleointensity behavior of natural minerals. *Journal of Geophysical Research*, 110(B1). <https://doi.org/10.1029/2004jb003095>
- Geologic Materials Center. (2015). Alaska Department of Natural Resources, Division of Geological and Geophysical Surveys, Anchorage, Alaska. Retrieved from <https://maps.dggs.alaska.gov/gmc/>
- George, R. (2004). Chemical versus temporal controls on the evolution of tholeiitic and calc-alkaline magmas at two volcanoes in the Alaska-Aleutian arc. *Journal of Petrology*, 45(1), 203–219. <https://doi.org/10.1093/petrology/egg086>
- Hillhouse, J. W., & Grommé, C. S. (1980). Paleomagnetism of the Triassic Hound island volcanics, Alexander terrane, southeastern Alaska. *Journal of Geophysical Research*, 85(B5), 2594. <https://doi.org/10.1029/jb085ib05p02594>
- Hubbard, B. (1931). A world inside a mountain. *National Geographic Society*, 60(3), 319–345.
- Jicha, B. R., Scholl, D. W., Singer, B. S., Yagodinski, G. M., & Kay, S. M. (2006). Revised age of Aleutian Island Arc formation implies high rate of magma production. *Geology*, 34(8), 661. <https://doi.org/10.1130/g22433.1>
- Johnson, C. L., Constable, C. G., Tauxe, L., Barendregt, R., Brown, L. L., Coe, R. S., et al. (2008). Recent investigations of the 0–5 Ma geomagnetic field recorded by lava flows. *Geochemistry, Geophysics, Geosystems*, 9(4). <https://doi.org/10.1029/2007gc001696>
- Korte, M., & Constable, C. (2011). Improving geomagnetic field reconstructions for 0–3 ka. *Physics of the Earth and Planetary Interiors*, 188(3–4), 247–259. <https://doi.org/10.1016/j.pepi.2011.06.017>
- Korte, M., Constable, C., Donadini, F., & Holme, R. (2011). Reconstructing the Holocene geomagnetic field. *Earth and Planetary Science Letters*, 312(3–4), 497–505. <https://doi.org/10.1016/j.epsl.2011.10.031>
- Korte, M., Donadini, F., & Constable, C. G. (2009). Geomagnetic field for 0–3 ka: 2. A new series of time-varying global models. *Geochemistry, Geophysics, Geosystems*, 10(6). <https://doi.org/10.1029/2008gc002297>
- LisÉ-Pronovost, A., St-Onge, G., Brachfeld, S., Barletta, F., & Darby, D. (2009). Paleomagnetic constraints on the Holocene stratigraphy of the Arctic Alaskan margin. *Global and Planetary Change*, 68(1–2), 85–99. <https://doi.org/10.1016/j.gloplacha.2009.03.015>

- McGimsey, R. G., Waythomas, C. F., & Neal, C. A. (1994). High stand and catastrophic draining of intracaldera Surprise Lake, Aniakchak Volcano, Alaska: A section in Geologic Studies in Alaska by the U.S. Geological Survey, 1993. *U.S. Geological Survey Bulletin*, 2109, 59–71. <https://doi.org/10.3133/70180217>
- Miller, T. P., & Smith, R. L. (1977). Spectacular mobility of ash flows around Aniakchak and Fisher calderas, Alaska. *Geology*, 5(3), 173. [https://doi.org/10.1130/0091-7613\(1977\)5<173:SMOFAFA>2.0.CO;2](https://doi.org/10.1130/0091-7613(1977)5<173:SMOFAFA>2.0.CO;2)
- Miller, T. P., & Smith, R. L. (1987). Late Quaternary caldera-forming eruptions in the eastern Aleutian arc, Alaska. *Geology*, 15(5), 434. [https://doi.org/10.1130/0091-7613\(1987\)15<434:LQCEIT>2.0.CO;2](https://doi.org/10.1130/0091-7613(1987)15<434:LQCEIT>2.0.CO;2)
- Nagata, T., Arai, Y., & Momose, K. (1963). Secular variation of the geomagnetic total force during the last 5000 years. *Journal of Geophysical Research*, 68(18), 5277–5281. <https://doi.org/10.1029/j.2156-2202.1963.tb00005.x>
- Neal, C. A., McGimsey, R. G., Braitseva, O., Miller, T. P., Eichelberger, J. C., & Nye, C. (1992). Postcaldera eruptive history of Aniakchak caldera, Alaska. *Eos*, 73(43), 645.
- Neal, C. A., McGimsey, R. G., Miller, T. P., Riehle, J. R., Waythomas, C. F., (2000). Preliminary volcano-hazard assessment for Aniakchak volcano, Alaska. *US Geological Survey Open-File Report 00-519* (p. 35). <https://doi.org/10.3133/ofr00519>
- Nicholson, R. S., Gardner, J. E., & Neal, C. A. (2011). Variations in eruption style during the 1931 A.D. eruption of Aniakchak volcano, Alaska. *Journal of Volcanology and Geothermal Research*, 207(3–4), 69–82. <https://doi.org/10.1016/j.jvolgeores.2011.08.002>
- Nilsson, A., Holme, R., Korte, M., Suttie, N., & Hill, M. (2014). Reconstructing Holocene geomagnetic field variation: New methods, models and implications. *Geophysical Journal International*, 198(1), 229–248. <https://doi.org/10.1093/gji/ggu120>
- Packer, D. R., & Stone, D. B. (1974). Paleomagnetism of Jurassic Rocks from Southern Alaska, and the Tectonic Implications. *Canadian Journal of Earth Sciences*, 11(7), 976–997. <https://doi.org/10.1139/e74-095>
- Paterson, G. A. (2011). A simple test for the presence of multidomain behavior during paleointensity experiments. *Journal of Geophysical Research*, 116(B10). <https://doi.org/10.1029/2011jb008369>
- Paterson, G. A., Tauxe, L., Biggin, A. J., Shaar, R., & Jonestrask, L. C. (2014). On improving the selection of Thellier-type paleointensity data. *Geochemistry, Geophysics, Geosystems*, 15(4), 1180–1192. <https://doi.org/10.1002/2013gc005135>
- Pavón-Carrasco, F. J., Osete, M. L., Torta, J. M., & De Santis, A. (2014). A geomagnetic field model for the Holocene based on archaeomagnetic and lava flow data. *Earth and Planetary Science Letters*, 388, 98–109. <https://doi.org/10.1016/j.epsl.2013.11.046>
- Pearce, C., Varhelyi, A., Wastegård, S., Muschitiello, F., Barrientos, N., O'Regan, M., et al. (2017). The 3.6 ka Aniakchak tephra in the Arctic Ocean: A constraint on the Holocene radiocarbon reservoir age in the Chukchi Sea. *Climate of the Past*, 13(4), 303–316. <https://doi.org/10.5194/cp-13-303-2017>
- Shaar, R., & Tauxe, L. (2013). Thellier GUI: An integrated tool for analyzing paleointensity data from Thellier-type experiments. *Geochemistry, Geophysics, Geosystems*, 14(3), 677–692. <https://doi.org/10.1002/ggge.20062>
- Smith, W. R. (1925). Aniakchak Crater, Alaska Peninsula. *U.S. Geological Survey Professional Paper 132-J*. (pp. 139–145). <https://doi.org/10.3133/pp132j>
- Stamatatos, J. A., Trop, J. M., & Ridgway, K. D. (2001). Late Cretaceous paleogeography of Wrangellia: Paleomagnetism of the MacColl Ridge Formation, southern Alaska, revisited. *Geology*, 29(10), 947. [https://doi.org/10.1130/0091-7613\(2001\)029<0947:lcpowp>2.0.co;2](https://doi.org/10.1130/0091-7613(2001)029<0947:lcpowp>2.0.co;2)
- Stone, D. B., & Layer, P. W. (2006). Paleosecular variation and GAD studies of 0–2 Ma flow sequences from the Aleutian Islands, Alaska. *Geochemistry, Geophysics, Geosystems*, 7(4). <https://doi.org/10.1029/2005gc001007>
- Stone, D. B., & Packer, D. R. (1979). Paleomagnetic data from the Alaska Peninsula. *Geological Society of America Bulletin*, 90(6), 545. [https://doi.org/10.1130/0016-7606\(1979\)90<545:PDFTAP>2.0.CO;2](https://doi.org/10.1130/0016-7606(1979)90<545:PDFTAP>2.0.CO;2)
- Symonds, R. B., Poreda, R. J., Evans, W. C., Janik, C. J., & Ritchie, B. E. (2003). Mantle and crustal sources of carbon, nitrogen, and noble gases in Cascade-Range and Aleutian-Arc volcanic gases. *U.S. Geological Survey Open-File Report 2003–436* (p. 26). <https://doi.org/10.3133/ofr03436>
- Tauxe, L., Shaar, R., Jonestrask, L., Swanson-Hysell, N. L., Minnett, R., Koppers, A. A. P., et al. (2016). PmagPy: Software package for paleomagnetic data analysis and a bridge to the Magnetics Information Consortium (MagIC) Database. *Geochemistry, Geophysics, Geosystems*, 17(6), 2450–2463. <https://doi.org/10.1002/2016gc006307>
- Tauxe, L., & Staudigel, H. (2004). Strength of the geomagnetic field in the Cretaceous Normal Superchron: New data from submarine basaltic glass of the Troodos Ophiolite. *Geochemistry, Geophysics, Geosystems*, 5(2). <https://doi.org/10.1029/2003gc000635>
- Thrupp, G. A., & Coe, R. S. (1986). Early Tertiary paleomagnetic evidence and the displacement of southern Alaska. *Geology*, 14(3), 213. [https://doi.org/10.1130/0091-7613\(1986\)14<213:ETPEAT>2.0.CO;2](https://doi.org/10.1130/0091-7613(1986)14<213:ETPEAT>2.0.CO;2)
- VanderHoek, R. (2009). *The role of ecological barriers in the development of cultural boundaries during the later Holocene of the central Alaska Peninsula* (Ph.D. dissertation). University of Illinois at Urbana-Champaign.
- VanderHoek, R., & Myron, R. (2004). An archaeological overview and assessment of Aniakchak National Monument and Preserve. *U.S. National Park Service Research/Resources Management Report*. AR/CRR-2004-47.
- Yu, Y., Tauxe, L., & Genevey, A. (2004). Toward an optimal geomagnetic field intensity determination technique. *Geochemistry, Geophysics, Geosystems*, 5(2). <https://doi.org/10.1029/2003gc000630>